Dynamic-Decoupled Active Damping Control Method for Improving Current Transient Behavior of LCL-Equipped High-Speed PMSMs

Yao, Yu; Huang, Yunkai; Peng, Fei; Dong, Jianning; Zhu, Zichong

DOI
10.1109/TPEL.2021.3109157

Publication date
2022

Document Version
Final published version

Published in
IEEE Transactions on Power Electronics

Dynamic-Decoupled Active Damping Control Method for Improving Current Transient Behavior of *LCL*-Equipped High-Speed PMSMs

Yu Yao, *Student Member, IEEE*, Yunkai Huang, Fei Peng, *Member, IEEE*, Jianning Dong, *Member, IEEE*, and Zichong Zhu, *Student Member, IEEE*

***Abstract*—In this article, a novel dynamic-decoupled active damping current controller is proposed for an *LCL*-equipped high-speed permanent magnet synchronous machine. Compared with the conventional stationary current-control method for the *LCL*-type system, the proposed method is established in the synchronous rotating frame for improving the current transient performance. When taking the controller into the synchronous coordinate, there are two following challenges: first, the synchronous resonance frequency varying in a wide range because of the synchronous coordinate transformation, and second, eliminating the coupling between the *dq* coordinate. To address these issues, an improved synchronous capacitor-current-feedback active damping method is designed based on arbitrary pole assignment and is significantly effective for the *LCL* resonance within the Nyquist frequency. Moreover, a novel dynamic-decoupled motor-current controller is proposed to eliminate the coupling between the *dq*-axis motor current. The gain selection method is discussed to acquire sufficient phase margin and gain margin. Finally, the effectiveness of the proposed method is verified by driving the tested motor to 72 kr/min.**

***Index Terms*—Active damping (AD), capacitor-current feedback, dynamic decoupling, high-speed surface-mounted permanent magnet synchronous machine (HSPMSM), synchronous rotating frame.**

I. Introduction

HIGH-SPEED surface-mounted permanent magnet synchronous machines (HSPMSMs) are widely used in the industrial applications because of its high power density and high efficiency [1]. Because of the small motor inductance, the high current ripple occurs in the winding current resulting from the limited pulsewidth modulation (PWM) frequency. Inevitably, it brings additional losses on the stator and, thus, the system efficiency is reduced. To eliminate the current ripple, an additional output *LCL* filter is preferred between the inverter and the machine. However, the resonance caused by the *LCL* circuit is introduced and the resonance damping strategy should be adopted for stabilizing the current control loop.

Significant research efforts have been established to develop active damping (AD) strategies to effectively deal with this resonance problem, which can be classified into following categories: inherent damping (ID) [2]–[5], filter-based method [6]–[9], virtual-resistance method [9]–[12], and full-state feedback control method [13]–[18]. In the full-digital control system, the digital-time computation delay and the PWM delay introduce the ID into the current control loop and it will stabilize the single-loop system [4]. The selection of the feedback loop relies on the location of the resonance frequency [2]. In the unstable region of ID, the extra AD control is necessary.

The virtual-resistance AD method is popularly used, which is derived from the passive damping (PD). But the real damping resistance in the PD is replaced by the virtual resistance, which is induced by the extra feedback loop. A virtual resistance in parallel with the capacitor can be achieved by the proportional capacitor-current feedback [10]. But due to the digital computation delay and PWM delay, the proportional capacitor-current feedback will be ineffective as the virtual resistance becomes negative when the *LCL* resonance crosses through the critical frequency (i.e., one-sixth of the sampling frequency, $f_s/6$) resulting from the parameter variation [19]. To address this issue, Pan *et al.* [20] propose a reduced computation delay method by shifting the capacitor current sampling instant. Wang *et al.* [21] and Li *et al.* [22] modify the capacitor-current-feedback loop to increase the critical frequency to $f_s/4$ and $f_s/3$, respectively. To achieve stable AD when the *LCL* resonance locates within the Nyquist frequency ($f_s/2$), Pan *et al.* [23] propose an optimal capacitor-current-feedback coefficient selection method, but it relies on the location of the *LCL* resonance under the zero grid inductance. In [24], a proportional–integral (PI) capacitor-current feedback is introduced. Among these methods, they are established in the stationary coordinate for the grid-connected inverter (i.e.,

Manuscript received May 23, 2021; revised August 13, 2021; accepted August 28, 2021. Date of publication September 1, 2021; date of current version November 30, 2021. This work was supported in part by the National Natural Science Foundation of China under Grants 51777034 and 51707037 and in part by the Excellence Project Funds of Southeast University. Recommended for publication by Associate Editor B. Mirafzal. *(Corresponding author: Yunkai Huang.)*

Yu Yao, Yunkai Huang, and Fei Peng are with the School of Electrical Engineering, Southeast University, Nanjing 210096, China (e-mail: yuyao@seu.edu.cn; huangyk@seu.edu.cn; pengfei@seu.edu.cn).

Jianning Dong is with the Delft University of Technology, 2628 CD Delft, The Netherlands (e-mail: j.dong-4@tudelft.nl).

Zichong Zhu is with the School of Electrical Engineering and Control Science, Nanjing Tech University, Nanjing 211816, China (e-mail: zichong_zhu@seu.edu.cn).

Color versions of one or more figures in this article are available at https://doi.org/10.1109/TPEL.2021.3109157.

Digital Object Identifier 10.1109/TPEL.2021.3109157

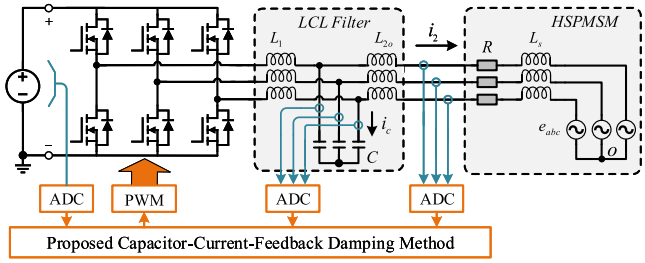

Fig. 1. System diagram of the HSPMSM drives equipped with *LCL* filter.

the fundamental frequency is unchanged) and the injected grid current is controlled by a proportional-resonant (PR) controller.

For the *LCL*-equipped HSPMSM drive, the fundamental frequency (f_e) is relatively high (>1 kHz) and fast changed during the speed-dynamic process. The transient performance of the current control is difficult to be guaranteed if a PR controller is implemented in the stationary coordinate. Therefore, the dq-axis current controller is preferred for the HSPMSM drives to achieve the field-oriented control (FOC). When taking the current controller into the synchronous rotating frame, one challenge is eliminating the coupling between the dq coordinate to improve the transient behavior. Because of the high fundamental frequency, the coupling items between the dq coordinate deteriorate the current dynamic response. The other challenge is that the resonance frequency in the dq coordinate varies a wide range resulting from the synchronous transformation. In that case, the synchronous resonance frequency moves across the critical frequency easily. Therefore, an effective synchronous capacitor-current-feedback AD method within the Nyquist frequency is essential for the *LCL*-equipped HSPMSM drives.

To solve the aforementioned problems, this article proposes a novel dynamic-decoupled capacitor-current-feedback AD current controller for *LCL*-equipped HSPMSM drives in the synchronous rotating frame. The proposed current control method has the following advantages.

1) Improved synchronous capacitor-current-feedback AD method where the damping performance can be designed with more freedom (i.e., the desired resonance frequency and the damping constant).
2) Effective for the *LCL* resonance frequency within the Nyquist frequency ($f_s/2$).
3) Enhanced dynamic decoupling capability to improve the transient performance compared with the conventional PI decoupled method.

Finally, the effectiveness of the proposed method is verified by driving the tested HSPMSM up to 72 kr/min (1200 Hz).

II. Discrete-Time Model in Synchronous Rotating Frame

A. Discrete-Time Model

Fig. 1 shows the system diagram of the HSPMSM drive equipped with an *LCL* filter, where ADC denotes the analog-to-digital converter. The complex continuous-time transfer function of the capacitor current in the $\alpha\beta$ stationary coordinate is derived as

$$G_{i_c}^s(s) = \frac{i_{cs}(s)}{V_s(s)} = \frac{1}{sL_1}\frac{s^2}{s^2+\omega_{\text{res}}^2} \tag{1}$$

where $\omega_{\text{res}} = 2\pi f_{\text{res}} = \sqrt{(L_1+L_2)/(L_1L_2\,C)}$ is the natural resonant frequency. L_1 is the inverter-side inductance. $L_2 = L_{2o} + L_s$. L_{2o} is the motor-side inductance. L_s is the motor inductance. C refers to the filtered capacitor. $i_{cs} = i_{c\alpha} + ji_{c\beta}$ is the capacitor current and $V_s = V_{2\alpha} + jV_{2\beta}$ denotes the inverter output voltage. The back electromotive force is neglected, since it only influences the fundamental motor current and has no effect on stability [10]. With zero-order hold method, the discrete-time transfer function can be obtained as

$$G_{i_c}^s(z) = \frac{i_{cs}(z)}{V_s(z)} = \frac{\sin(\omega_{\text{res}}T)}{\omega_{\text{res}}L_1}\frac{z-1}{z^2-2z\cos(\omega_{\text{res}}T)+1} \tag{2}$$

where T is the sampling period.

The transfer function of the capacitor current to the motor current is given as

$$G_{i_2}^s(s) = \frac{i_{2r}(s)}{i_{cr}(s)} = \frac{1}{sC}\frac{1}{sL_2+R} \tag{3}$$

where R is the motor resistance. By using an impulse-invariant discretization method, it leads to

$$G_{i_2}^s(z) = \frac{i_{2r}(z)}{i_{cr}(z)} = \frac{\kappa z}{(z-1)(z-e^{-R/L_2T})} \tag{4}$$

where κ is defined as

$$\kappa = \frac{T}{RC}(1-e^{-\frac{R}{L_2}T}). \tag{5}$$

To achieve better current transient response, the current controller should be established in the dq synchronous coordinate. To represent the transfer function in the dq synchronous coordinate, the frequency shift $z \to ze^{j\omega_eT}$ is applied in (2) and (4), which leads to

$$G_{i_c}(z) = \frac{i_{cr}(z)}{V_r(z)} = \frac{\sin(\omega_{\text{res}}T)}{\omega_{\text{res}}L_1} \times \frac{ze^{j\omega_eT}-1}{z^2e^{2j\omega_eT}-2ze^{j\omega_eT}\cos(\omega_{\text{res}}T)+1} \tag{6}$$

$$G_{i_2}(z) = \frac{i_{2r}(z)}{i_{cr}(z)} = \frac{\kappa ze^{j\omega_eT}}{(ze^{j\omega_eT}-1)(ze^{j\omega_eT}-e^{-\frac{R}{L_2}T})} \tag{7}$$

where $i_{cr} = i_{cd} + ji_{cq}$. $V_r = V_d + jV_q$. $\omega_e = 2\pi f_e$ is the fundamental angular frequency, where f_e is the fundamental frequency.

B. Digital-Delay Modeling

Fig. 2 shows the diagram of the voltage reference calculation and PWM update. $V_r^*(k)$ is the digital voltage reference vector in the synchronous coordinate. $V_s^*(k)$ denotes the digital voltage reference vector in the stationary $\alpha\beta$ coordinate.

Besides, on basis of Fig. 2, there is

$$V_s^*(k) = V_r^*(k)e^{j(\theta(k)+\omega_e(k)T)} \tag{8}$$

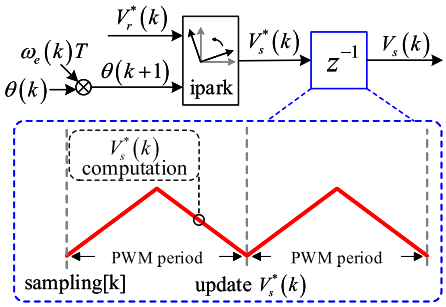

Fig. 2. Diagram of voltage reference calculation and PWM update.

and there exists one-sampling-period delay between the stationary voltage reference and the actual stationary voltage as

$$V_s^*(k) = V_s(k+1). \tag{9}$$

Besides, considering the synchronous transformation of the actual output voltage, it leads to

$$V_s(k+1) = V_r(k+1)e^{j\theta(k+1)}. \tag{10}$$

Based on (8)–(10)

$$\begin{aligned} V_r^*(k) &= V_s^*(k)e^{-j(\theta(k)+\omega_e(k)T)} \\ &= V_s(k+1)e^{-j(\theta(k)+\omega_e(k)T)} \\ &= V_r(k+1)e^{j(\theta(k+1)-\theta(k)-\omega_e(k)T)}. \end{aligned} \tag{11}$$

Considering $\theta(k+1) = \theta(k) + \omega_e(k)T$, (11) can be simplified as

$$V_r^*(k) = V_r(k+1). \tag{12}$$

It should be noted that the pure one-sampling-period delay in the synchronous reference frame is achieved by the reference calculation method, as shown in Fig. 2. The coupling of the synchronous coordinate resulting from the digital delay is eliminated compared with Kim *et al.* [25]. Therefore, the synchronous discrete-time model with digital delay is derived as

$$G_p(z) = \frac{i_{2r}(z)}{V_r^*(z)} = z^{-1}G_{i_c}(z)G_{i_2}(z) \tag{13}$$

where V_r^* denotes the complex voltage reference.

C. Synchronous Resonance Frequency

Fig. 3 shows the bode diagram of the open-loop transfer function. f_N is the rated fundamental frequency. f_s is the sampling frequency. It can be checked that the resonant frequency in the synchronous coordinate varies with f_e as

$$f_{\text{res}}^r = f_{\text{res}} - f_e \tag{14}$$

where f_{res}^r denotes the synchronous resonance frequency.

According to the discrete-time model $G_p(z)$, as shown in (3), the phase before the synchronous resonance frequency can be calculated as

$$\angle G_p(z = e^{-j\omega T}) = -\frac{\pi}{2} - \frac{3}{2}\omega T - \frac{1}{2}\omega_e T \tag{15}$$

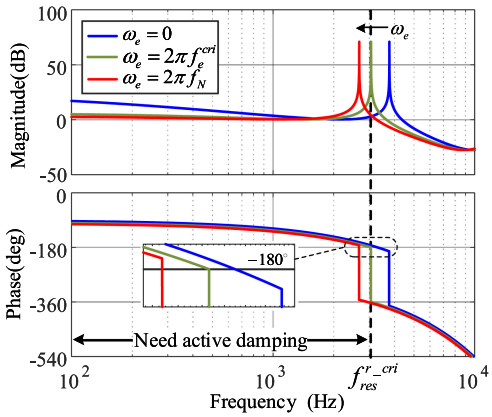

Fig. 3. Bode diagram of the discrete-time model in the synchronous rotating frame. $f_N = 1200$ Hz, $f_{\text{res}} = 3875$ Hz, and $f_s = 20$ kHz.

TABLE I
PARAMETERS OF THE EXPERIMENTAL PLANT

Symbol	Parameter	Value
R	winding resistance	0.045Ω
L_1	inductance at the inverter side	54μH
L_{2o}	inductance at the machine side	27.5μH
L_s	machine inductance (SPMSM)	24μH
C_1	capacitor of LCL filter	64μF
f_{res}	resonant frequency	3875Hz
$poles$	poles of the machine	2
f_s	switching frequency	20kHz
T	sampling period	50μs
n_N	the rated speed	72kr/min
f_N	the rated fundamental frequency	1200 Hz

and the $-180°$ crossover frequency can be derived as

$$f_{-180°} = \frac{f_s}{6} - \frac{f_e}{3}. \tag{16}$$

Based on (14) and (16), the critical fundamental frequency where f_{res}^r is equal to $f_{-180°}$ can be derived as

$$f_e^{\text{cri}} = \frac{3}{2}\left(f_{\text{res}} - \frac{f_s}{6}\right) \tag{17}$$

and in that case, the critical synchronous frequency can be expressed as

$$f_{\text{res}}^{r\_\text{cri}} = \frac{1}{4}\left(f_s - 2f_{\text{res}}\right). \tag{18}$$

Therefore, in this article, according to Table I, the critical fundamental frequency f_e^{cri} and the critical synchronous resonance frequency can be calculated as

$$f_e^{\text{cri}} = 813 \quad f_{\text{res}}^{r\_\text{cri}} = 3062. \tag{19}$$

In Fig. 3, when the machine is running at low speed, the fundamental frequency f_e is lower than the critical frequency (813 Hz) and in that case, $-180°$ crossing at the resonance frequency is avoided. No extra AD strategy is needed. But when the machine is running at high speed, f_e is larger than the critical frequency (813 Hz) and $-180°$ crossing at the resonance frequency occurs. Therefore, a wide-frequency-range effective synchronous capacitor-current feedback is essential for the *LCL*-equipped HSPMSM drives.

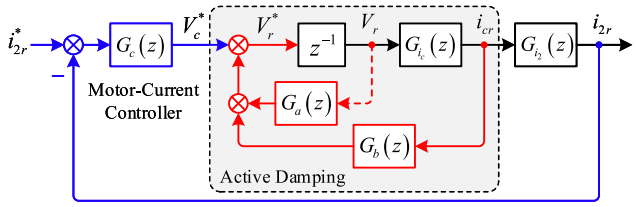

Fig. 4. Control structure of the proposed synchronous capacitor-current-feedback AD method and motor-current controller.

III. Proposed Synchronous Capacitor-Current-Feedback AD

Fig. 4 shows the control structure of the proposed method, which can be expressed as

$$V_r^*(z) = G_c(z)(i_{2r}^* - i_{2r}) + G_a(z)V_r + G_b(z)i_{cr} \tag{20}$$

where i_{2r}^* is the current reference. $G_c(z)$, $G_a(z)$, and $G_b(z)$ are the transfer function of the motor-current controller, output voltage feedback, and capacitor-current feedback, respectively. It should be noted that V_r can be obtained by delaying the voltage reference V_r^* and, thus, no additional sensors are needed compared with the conventional capacitor-current-feedback methods.

A. AD Feedback Loop Design

The transfer function of the output voltage feedback and the capacitor-current feedback are designed as

$$G_a(z) = \frac{a_1 z + a_2}{\gamma_1 z + \gamma_2} \quad G_b(z) = \frac{b_1 z + b_2}{\gamma_1 z + \gamma_2} \tag{21}$$

where γ_1, γ_2, a_1, a_2, b_1, and b_2 are the coefficients, which will be discussed later.

The transfer function from V_c^* to i_{cr} can be obtained as

$$\begin{aligned} G_{\text{der}}(z) &= \frac{i_{cr}(z)}{V_c^*(z)} = \frac{P(z)}{Q(z)} \\ &= \frac{z^{-1}G_{i_c}(z)}{1 - z^{-1}G_a(z) - z^{-1}G_{i_c}(z)G_b(z)} \end{aligned} \tag{22}$$

where $G_{\text{der}}(z)$ denotes the internal damped transfer function from the output voltage to the capacitor current. V_c^* is the output of the motor-current controller. Substituting (6) and (21) into (22), it leads to

$$\begin{aligned} G_{\text{der}}(z) &= \frac{P(z)}{Q(z)} \\ &= \frac{(\gamma_1 z + \gamma_2)\, N(z)}{(z\,(\gamma_1 z + \gamma_2) - (a_1 z + a_2))\, D(z) - (b_1 z + b_2)\, N(z)} \end{aligned} \tag{23}$$

where $N(z)$ and $D(z)$ are defined as

$$\begin{aligned} N(z) &= \frac{\sin(\omega_{\text{res}} T)}{\omega_{\text{res}} L_1}\left(z e^{j\omega_e T} - 1\right) \\ D(z) &= z^2 e^{2j\omega_e T} - 2z e^{j\omega_e T}\cos(\omega_{\text{res}} T) + 1. \end{aligned} \tag{24}$$

It should be noted that the degree of $Q(z)$ is 4 and it contains 6 coefficients, which indicates $Q(z)$ can be designed flexibly by the appropriate coefficient selection.

$Q(z)$ can be rewritten as

$$\begin{aligned} Q(z) =\ & (z\,(\gamma_1 z + \gamma_2) - (a_1 z + a_2))\, D(z) \\ & - (b_1 z + b_2)\, N(z) \\ =\ & \alpha_4 z^4 + \alpha_3 z^3 + \alpha_2 z^2 + \alpha_1 z + \alpha_0 \end{aligned} \tag{25}$$

where α_i $(i = 1, 2, 3, 4)$ is defined as

$$\begin{aligned} \alpha_4 &= \gamma_1 e^{2j\omega_e T} \\ \alpha_3 &= (\gamma_2 - a_1)\, e^{2j\omega_e T} - 2\gamma_1 e^{j\omega_e T}\cos(\omega_{\text{res}} T) \\ \alpha_2 &= \gamma_1 - 2(\gamma_2 - a_1)\, e^{j\omega_e T}\cos(\omega_{\text{res}} T) - a_2 e^{2j\omega_e T} \\ &\quad - \frac{\sin(\omega_r T)}{\omega_{\text{res}} L_1} b_1 e^{2j\omega_e T} \\ \alpha_1 &= (\gamma_2 - a_1) + 2a_2 e^{j\omega_e T}\cos(\omega_r T) \\ &\quad - \frac{\sin(\omega_r T)}{\omega_r L_1}\left(b_2 e^{j\omega_e T} - b_1\right) \\ \alpha_0 &= -a_2 + \frac{\sin(\omega_r T)}{\omega_r L_1} b_2. \end{aligned} \tag{26}$$

Besides, the desired $Q(z)$ is given as

$$\overline{Q}(z) = (\gamma_1 z + \gamma_2) z\left(z^2 e^{2j\omega_e T} - 2z e^{j\omega_e T}\cos(\overline{\omega}_{\text{res}} T) + \delta\right) \tag{27}$$

where $\overline{\omega}_{\text{res}} = 2\pi \overline{f}_{\text{res}}$ denotes the desired resonance angular frequency and $\overline{f}_{\text{res}}$ is the desired resonance frequency. δ is a damping constant, which is less than 1. The desired $Q(z)$ is expanded as

$$\overline{Q}(z) = \beta_4 z^4 + \beta_3 z^3 + \beta_2 z^2 + \beta_1 z + \beta_0 \tag{28}$$

where these coefficients β_i $(i = 1, 2, 3, 4)$ are defined as

$$\begin{aligned} \beta_4 &= \gamma_1 e^{2j\omega_e T} \\ \beta_3 &= \gamma_2 e^{2j\omega_e T} - 2\gamma_1 e^{j\omega_e T}\cos(\overline{\omega}_{\text{res}} T) \\ \beta_2 &= \gamma_1 \delta - 2\gamma_2 e^{j\omega_e T}\cos(\overline{\omega}_{\text{res}} T) \\ \beta_1 &= \gamma_2 \delta \\ \beta_0 &= 0. \end{aligned} \tag{29}$$

To achieve $Q(z) = \overline{Q}(z)$, $\alpha_i = \beta_i$ $(i = 1, 2, 3, 4)$ should be satisfied and it leads to

$$\begin{aligned} a_1 &= 2\gamma_1 e^{-j\omega_e T}\left(\cos(\overline{\omega}_{\text{res}} T) - \cos(\omega_{\text{res}} T)\right) \\ a_2 &= \frac{\sin(\omega_{\text{res}} T)}{\omega_{\text{res}} L_1} b_2 \\ b_1 &= x e^{-j\omega_e T} - b_2 \\ b_2 &= \frac{y - x e^{-j\omega_e T}}{(2\cos(\omega_{\text{res}} T) - 1) e^{j\omega_e T} - 1} \end{aligned} \tag{30}$$

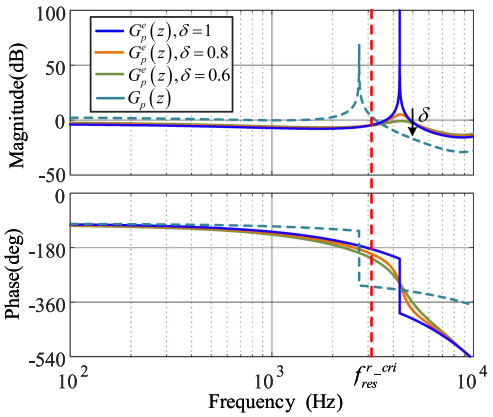

Fig. 5. Bode diagram of the damped model. f_e=1200 Hz and f_s=20 kHz. γ_1=1 and γ_2=−0.3. $\overline{f}_{\text{res}}$=5500 Hz. f_{res}=3875 Hz.

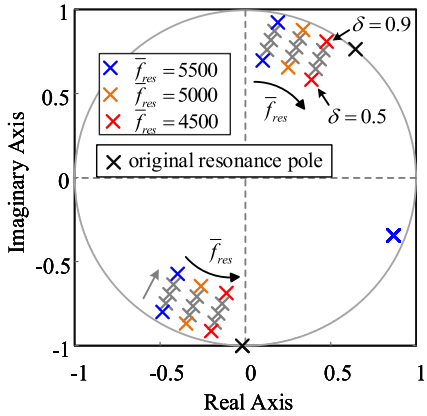

Fig. 6. Pole map of the damped model. f_e=1200 Hz. γ_1=1 and γ_2=−0.3. f_{res}=3875 Hz.

where x and y are defined as

$$x=\begin{bmatrix}\gamma_1\left(1-\delta\right)e^{-j\omega_e T}\\ +2\gamma_2\left(\cos\left(\overline{\omega}_{\text{res}}T\right)-\cos\left(\omega_{\text{res}}T\right)\right)\\ +2a_1\cos\left(\omega_{\text{res}}T\right)\end{bmatrix}\frac{\omega_{\text{res}}L_1}{\sin\left(\omega_{\text{res}}T\right)}$$

$$y=\left(a_1+\gamma_2(\delta-1)\right)\frac{\omega_{\text{res}}L_1}{\sin(\omega_{\text{res}}T)}. \tag{31}$$

It can be observed that a_1, a_2, b_1, and b_2 can be calculated based on aforementioned equation once γ_1 and γ_2 are selected. In that case, the damped transfer function is simplified with the desired $\overline{Q}(z)$ as

$$G_{\text{der}}(z)=\frac{(\gamma_1 z+\gamma_2)N(z)}{\overline{Q}(z)}. \tag{32}$$

B. Damped Model of the LCL-Equipped HSPMSM

When $|\gamma_2/\gamma_1|$ is less than 1, $\gamma_1 z+\gamma_2$ is stable and, thus, it can be simplified using zero-pole cancellation. In that way, G_{der} can be obtained as

$$G_{\text{der}}(z)=\frac{\sin\left(\omega_{\text{res}}T\right)}{\omega_{\text{res}}L_1}\times\frac{1}{z}\frac{ze^{j\omega_e T}-1}{z^2e^{2j\omega_e T}-2ze^{j\omega_e T}\cos\left(\overline{\omega}_{\text{res}}T\right)+\delta}. \tag{33}$$

Therefore, the damped discrete-time model with proposed AD is established as

$$G_p^e(z)=G_{\text{der}}(z)\times G_{i_2}(z)=\frac{\eta}{ze^{j\omega_e T}-e^{-\frac{R}{L_2}T}}\frac{e^{j\omega_e T}}{z^2e^{2j\omega_e T}-2ze^{j\omega_e T}\cos\left(\overline{\omega}_{\text{res}}T\right)+\delta} \tag{34}$$

where the coefficient η is defined as

$$\eta=\kappa\frac{\sin\left(\omega_{\text{res}}T\right)}{\omega_{\text{res}}L_1}. \tag{35}$$

Fig. 5 shows the bode diagram of the damped transfer function $G_p^e(z)$. f_e = 1200 Hz. The desired resonance frequency $\overline{f}_{\text{res}}$ = 5500 Hz. It can be observed that when δ = 1, the resonant frequency of the $G_p^e(z)$ moves to $\overline{f}_{\text{res}}$. As the decreasing δ, the resonant peak is well damped.

From the aspect of the pole map, as shown in Fig. 6, with the proposed AD method, the resonance pole pair can be arbitrarily assigned at the desired position by adjusting $\overline{f}_{\text{res}}$ and δ. Benefiting from this, the damping performance can be designed with more freedom. It is the main contribution compared with the conventional methods [10], [21].

C. Coefficient Selection

For the selection of the desired resonance frequency, there are two following considerations.

1) For the motor-current feedback system, the high *LCL* resonance is beneficial for stabilizing the current control loop [10]. In that case, the desired synchronous resonance frequency should be larger than $f_{\text{res}}^{r\_\text{cri}}$. Based on (14) and (18), $\overline{f}_{\text{res}}>\frac{2}{3}f_N+\frac{f_s}{6}$ should be satisfied.
2) When $\overline{f}_{\text{res}}$ is selected far away from the actual resonance frequency, the feedback transfer function $G_a(z)$ and $G_b(z)$ have to provide larger feedback output. Fig. 7 shows the bode diagram of $G_a(z)$ and $G_b(z)$ when the different $\overline{f}_{\text{res}}$ is selected. It can be easily observed that the magnitude of $G_a(z)$ and $G_b(z)$ increases with a large $\overline{f}_{\text{res}}$. In that case, the measurement noises of the capacitor current will deteriorate the control performance on the steady state.

Bear these in mind, to balance the stability and the suppression ability of the measurement noises, a coefficient η is introduced and the desired resonance frequency $\overline{f}_{\text{res}}$ can be selected based on (16) as

$$\overline{f}_{\text{res}}=\eta\left(\frac{2}{3}f_N+\frac{f_s}{6}\right). \tag{36}$$

To achieve more robustness, η is recommended from 1.05 to 1.25 in this article.

Besides, the damping constant δ can be selected more flexibly and it is recommended as

$$0.6<\delta<0.9. \tag{37}$$

Additionally, as the analysis mentioned earlier, $\gamma_1 z+\gamma_2$ should be stable. To simplify the coefficient selection, without

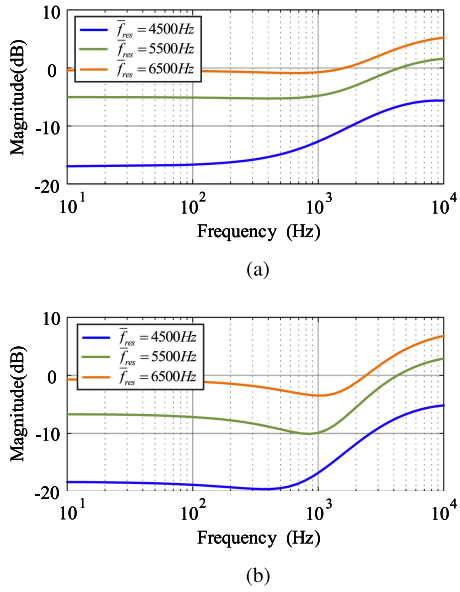

Fig. 7. Bode diagram of $G_a(z)$ and $G_b(z)$ when $\overline{f}_{\text{res}}$ is selected as 4500, 5500, and 6500 Hz. $f_e = 1200$ Hz. $\delta = 0.8$. $\gamma_1 = 1$ and $\gamma_2 = -0.3$. $f_{\text{res}} = 3875$ Hz. (a) Bode diagram of $G_a(z)$. (b) Bode diagram of $G_b(z)$.

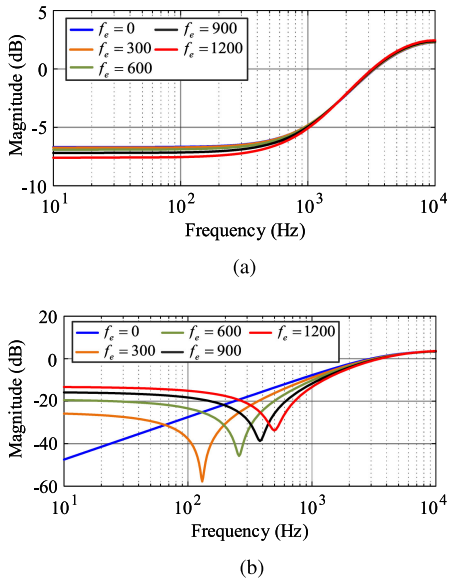

Fig. 8. Bode diagram of $G_a(z)$ and $G_b(z)$ when γ_2 is selected as (41). $\delta = 0.6$ and $\gamma_1 = 1$. $\overline{f}_{\text{res}} = 5500$ Hz. $f_{\text{res}} = 3875$ Hz. (a) Bode diagram of $G_a(z)$. (b) Bode diagram of $G_b(z)$.

loss of generality, γ_1 is selected as

$$\gamma_1 = 1. \tag{38}$$

For the coefficient γ_2, it should be selected to obtain a small magnitude of $G_b(z)$ and, thus, it enhances the suppression ability for the measurement noises of the capacitor current. From the aspect of this point, in this article, to simplify the coefficient selection, $|G_b(z = e^{j\omega T})|$ at zero speed is used to evaluate the selection of γ_2. Therefore, $|G_b(z)|$ at $\omega = 0$ can be described as

$$|G_b(z)|_{\omega=0} = \left|\frac{b_1 + b_2}{1 + \gamma_2}\right| = \frac{\omega_{\text{res}} L_1}{\sin(\omega_{\text{res}} T)} \left|\frac{D}{1 + \gamma_2}\right| \tag{39}$$

where D is defined as

$$D = 2\gamma_2 \left(\cos(\bar{\omega}_{\text{res}} T) - \cos(\omega_{\text{res}} T)\right) + (1 - \delta) + 4\left(\cos(\bar{\omega}_{\text{res}} T) - \cos(\omega_{\text{res}} T)\right)\cos(\omega_{\text{res}} T). \tag{40}$$

To obtain the smallest $|G_b(z)|$, γ_2 should be selected to achieve $D = 0$ as follows:

$$\gamma_2 = -\frac{1 - \delta}{2\left(\cos(\bar{\omega}_{\text{res}} T) - \cos(\omega_{\text{res}} T)\right)} - 2\cos(\omega_{\text{res}} T). \tag{41}$$

When γ_2 is selected as (41), the bode diagram of $G_a(z)$ and $G_b(z)$ is shown in Fig. 8. It can be observed that $G_a(z)$ and $G_b(z)$ stay at relatively low amplitude, even with the increasing f_e. Besides, it can be checked that $\gamma_1 z + \gamma_2$ is always stable when γ_2 is selected as (41).

IV. Dynamic-Decoupled Motor-Current Controller Design

As the mentioned analysis, the AD strategy has to be achieved with the proposed output-voltage and capacitor-current feedback. The equivalent control structure is shown in Fig. 9. To achieve FOC, the motor-current controller should be established

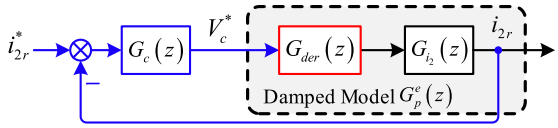

Fig. 9. Equivalent control structure.

in the synchronous rotating frame, but the damped model $G_p^e(z)$ contains the complex coefficient $e^{j\omega_e T}$, which indicates that there exists the dynamic coupling between the synchronous rotating frame when $\omega_e \neq 0$.

In this section, to achieve dynamic decoupling, the proposed motor-current controller is designed based on the zero-pole cancellation. After that, the gain selection method of the motor current controller is discussed.

A. Dynamic Decoupling

The equivalent discrete-time model with proposed AD $G_p^e(z)$ is rewritten as

$$G_p^e(z) = G_{pl}^e(z) \times G_{ph}^e(z) \tag{42}$$

where $G_{pl}^e(z)$ and $G_{ph}^e(z)$ are defined as

$$G_{pl}^e(z) = \frac{\eta}{z e^{j\omega_e T} - e^{-\frac{R}{L_2}T}}$$
$$G_{ph}^e(z) = \frac{e^{j\omega_e T}}{z^2 e^{2j\omega_e T} - 2z e^{j\omega_e T}\cos(\bar{\omega}_{\text{res}} T) + \delta}. \tag{43}$$

Fig. 10 shows the bode diagram of G_{ph}^e and G_{pl}^e when ω_e is selected as 0, πf_N, and $2\pi f_N$. $f_N = 1200$ Hz. It should be noted that when $\omega_e = 0$, there is no dynamic coupling. In other words, the coupling degree can be evaluated by the magnitude deviation with the case of $\omega_e = 0$. Bear this in the mind, the coupling analysis for $G_p^e(z)$ can be derived as follows.

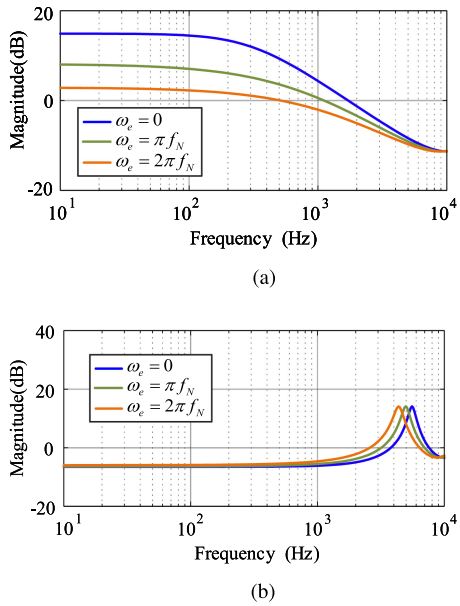

Fig. 10. Bode diagram of G^e_{ph} and G^e_{pl} when ω_e is selected as 0, πf_N, and $2\pi f_N$. $f_N = 1200$ Hz. $\overline{f}_{\text{res}} = 5500$ Hz. $\delta = 0.8$. (a) Bode diagram of G^e_{pl}. (b) Bode diagram of G^e_{ph}.

1) For G^e_{pl}, the magnitude is much decreased with the speed up and, thus, there exist a strong coupling between the synchronous rotating frame.
2) For G^e_{ph}, in the low-frequency region (less than 1 kHz), the magnitude deviation with the case of $\omega_e = 0$ is quite small. In the high-frequency region, the dynamic coupling still exists. Considering the exciting component located in the high-frequency region is usually small, the coupling caused by G^e_{ph} can be neglected.

Therefore, the dynamic coupling between the dq synchronous rotating frame mainly results from G^e_{pl}. To eliminate this coupling, the motor-current controller is designed as

$$G_c(z) = \frac{V_c^*(z)}{i^e_{2r}(z)} = \frac{ze^{j\omega_e T} - e^{-\frac{R}{L_2}T}}{z-1} \times \frac{az+b}{z-1} \tag{44}$$

where $i^e_{2r}(z) = i^*_{2r}(z) - i_{2r}(z)$, which is the regulated current error. a and b are controller parameters, which meet

$$a > 0, \quad -\frac{b}{a} \lesssim 1. \tag{45}$$

With the proposed motor-current controller, the open-loop transfer function is derived as

$$\begin{aligned}\frac{i_{2r}(z)}{i^e_{2r}(z)} &= G_c(z)G_{der}(z)G_{i_2}(z) \\ &= \underbrace{\frac{\eta(az+b)}{z^2-2z+1}}_{G_l(z)} \underbrace{\frac{e^{j\omega_e T}}{z^2e^{2j\omega_e T} - 2ze^{j\omega_e T}\cos(\overline{\omega}_{res}T) + \delta}}_{G^e_{ph}(z)}\end{aligned} \tag{46}$$

where $G_l(z)$ does not contain any complex coefficients and, thus, the coupling is eliminated.

B. Gain Determination

The selection method of the coefficient a and b is discussed to achieve desired PM and GM.

The magnitude and the phase of $G_l(z)$ is calculated as

$$\begin{aligned}|G_l(z)|(z = e^{-j\omega T}) &= \frac{\eta}{2\sin(\frac{\omega}{2}T)}\sqrt{a^2 + \left(\frac{a+b}{\omega T}\right)^2} \\ \angle G_l(z)(z = e^{-j\omega T}) &\approx -\frac{\pi}{2} - \frac{1}{2}\omega T - a\tan\left(\frac{a+b}{\omega T a}\right).\end{aligned} \tag{47}$$

Besides, the magnitude and the phase of $G^e_{ph}(z)$ is calculated as

$$\begin{aligned}|G^e_{ph}(z)|(z = e^{-j\omega T}) &= \frac{1}{\lambda_+(\omega,\omega_e)\lambda_-(\omega,\omega_e)} \\ \angle G^e_{ph}(z)(z = e^{-j\omega T}) &\approx -\omega T\end{aligned} \tag{48}$$

where $\lambda_+(\omega,\omega_e)$ and $\lambda_-(\omega,\omega_e)$ are defined as

$$\begin{aligned}\lambda_+(\omega,\omega_e) &= \sqrt{\delta - 2\sqrt{\delta}\cos(\omega T + \omega_e T + \rho) + 1} \\ \lambda_-(\omega,\omega_e) &= \sqrt{\delta - 2\sqrt{\delta}\cos(\omega T + \omega_e T - \rho) + 1} \\ \rho &= a\tan\left(\frac{\sqrt{\delta - \cos^2(\overline{\omega}_{\text{res}}T)}}{\cos(\overline{\omega}_{\text{res}}T)}\right).\end{aligned} \tag{49}$$

Proposition: To achieve PM$= \varphi$ and GM> -3 dB, the coefficient a and b of the linear controller should be selected on basis of the following equation:

$$\begin{aligned}a &= \frac{\lambda_+(\omega_{cp},\omega_e)\lambda_-(\omega_{cp},\omega_e)}{\eta}\omega_{cp}T \\ b &= a\left(\omega_{cp}\tan(\frac{\pi}{2} - \frac{3\omega_{cp}T}{2} - \varphi)T - 1\right)\end{aligned} \tag{50}$$

where ω_{cp} is the 0-dB gain crossing frequency and it can be selected by users. But the maximum value is limited as

$$\omega_{cp} < \frac{\sqrt{2}\pi}{6T}\frac{\lambda_+(\frac{\pi}{3T},\omega_e^m)\lambda_-(\frac{\pi}{3T},\omega_e^m)}{\lambda_+(0,\omega_e^m)\lambda_-(0,\omega_e^m)} \tag{51}$$

where ω_e^m is the maximum fundamental angular frequency, which is well predefined by users. The details on the proof of the proposition can be found in the Appendix. It should be noted that both $\lambda_+(\omega_{cp},\omega_e)$ and $\lambda_+(\omega_{cp},\omega_e)$ in (50) are related to ω_e and should be calculated online. To reduce the computation burden for the low-cost applications, the coefficient a can be selected approximately as

$$\hat{a} = \frac{\lambda_+(\omega_{cp},\omega_e^m)\lambda_-(\omega_{cp},\omega_e^m)}{\eta}\omega_{cp}T \tag{52}$$

where $\lambda_+(\omega_{cp},\omega_e^m)\lambda_-(\omega_{cp},\omega_e^m)$ can be calculated offline with the predefined ω_e^m, the damping constant δ, and the desired resonant frequency $\overline{\omega}_{\text{res}}$.

C. Numerical Test

Numerical tests are established to validate the effectiveness of the proposed motor current controller and the coefficient

TABLE II
PARAMETERS OF THE PROPOSED METHOD

Symbol	Parameter	Value
γ_1	coefficient	1
γ_2	coefficient	-0.5
δ	damping constant	0.8
$\overline{\omega}_{res}$	desired resonant frequency	$2\pi \times 5500$ rad/s
ω_{cp}	desired 0 dB crossing frequency	$2\pi \times 500$ rad/s
ω_e^m	maximum angular frequency	$2\pi \times 1200$ rad/s
φ	required PM	$\pi/3$

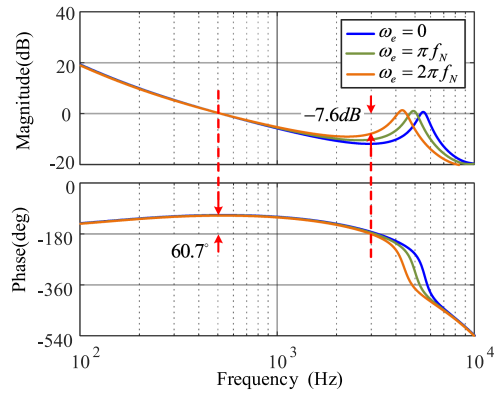

Fig. 11. Bode diagram of the open-loop transfer function with the proposed controller and the coefficient selection method in (50).

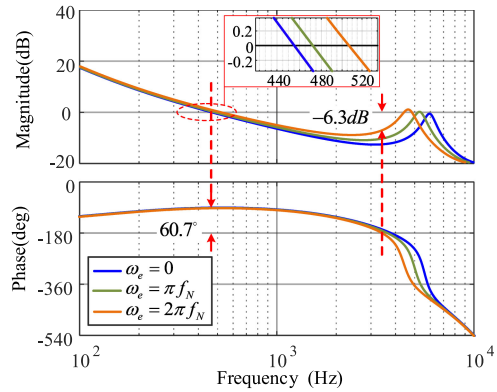

Fig. 12. Bode diagram of the open-loop transfer function with the proposed controller and the simplified coefficient selection method in (52).

selection method. The parameters of the *LCL* filter and the tested machine are shown in Table I. The parameters of the proposed method are shown in Table II. Based on (51), ω_{cp} is restricted as

$$\omega_{cp} < 2\pi \times 769.4\,\text{rad/s}. \tag{53}$$

Fig. 11 shows the bode diagram of the open-loop transfer function with the proposed controller and the coefficient selection method in (50). PM $= 60.7°$ and GM $= -7.6$ dB. Both the PM and GM are satisfied. In Fig. 12, the bode diagram of the open-loop transfer function with the simplified coefficient selection method in (52) is demonstrated. It can be observed that the 0-dB crossing frequency varies with ω_e. But the desired PM and the sufficient GM can be still achieved.

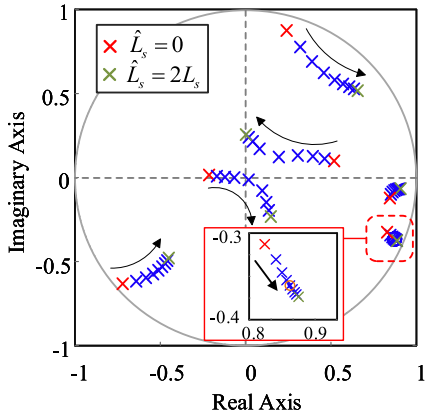

Fig. 13. Closed-loop pole map with the motor inductance L_s varying from 0% to 200% of the real value.

D. Robustness Against the Motor Inductance Variation

As well known, the motor inductance varies with the magnetic saturation. The robustness against the motor inductance variation of the proposed method should be evaluated well. Fig. 13 shows the close-loop pole map with the motor inductance L_s varying from 0% to 200% of the real value when the proposed current control method is implemented. All the closed-loop poles are still inside the unit cycle, which indicates the drive system is always stable.

V. SIMULATION VALIDATIONS AND ANALYSIS

To validate the effectiveness of the proposed wide-resonance-region AD method, simulations are performed in MATLAB/Simulink. The parameters of the experimental plant are shown in Table I. The parameters of the proposed method are shown in Table II.

A. Wide-Resonance-Region Performance

Fig. 14(a) shows the simulation result of the synchronous AD performance with the f_e ranging from 0 to 1.667 kHz. Correspondingly, the synchronous resonance frequency decreases from 3.57 to 2.2 kHz. Clearly, it moves across the critical synchronous resonance frequency 3.062 kHz based on (19). Therefore, based on the simulation results, the proposed method still works well, even when f_{res}^r varies in a wide range.

B. Comparison With Conventional Methods

Fig. 15 shows the control diagram of the conventional capacitor-current-feedback AD methods [10], [21]. In [10], the proportional capacitor-current feedback is adopted and in that case, the feedback transfer function $G_{cf}(z)$ is given as

$$G_{cf}(z) = k_c \tag{54}$$

where k_c is the feedback gain. Additionally, in [21], the capacitor-current feedback with a high-pass filter is adopted and in that case, the feedback transfer function $G_{cf}(z)$ is given as

$$G_{cf}(z) = \frac{ze^{j\omega_e T} - 1}{ze^{j\omega_e T} - 1 + 2\pi f_{hp} T} k_c \tag{55}$$

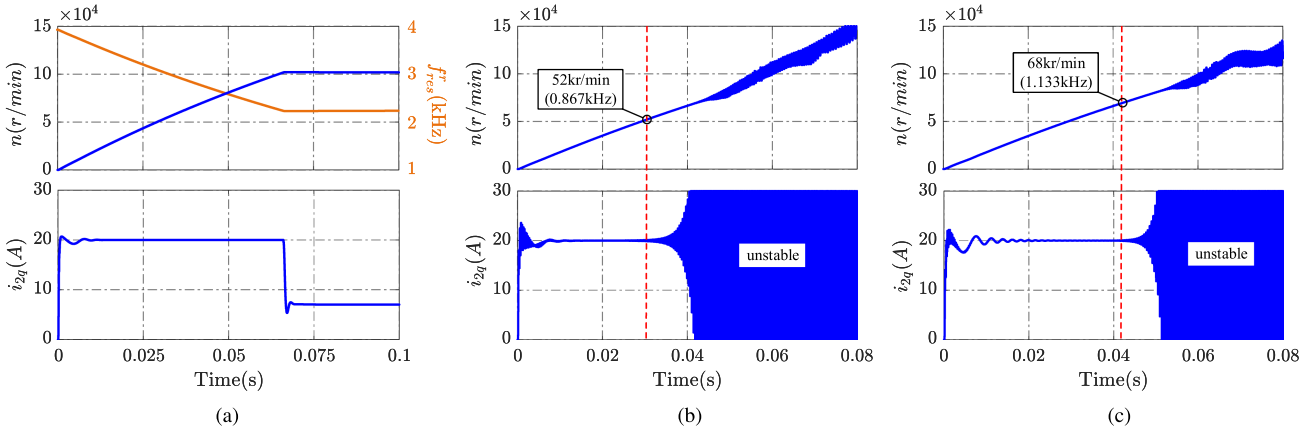

Fig. 14. Simulation results: wide-resonance-region performance comparison. (a) Proposed method. (b) Active damping method in [10]. (c) Active damping method in [21].

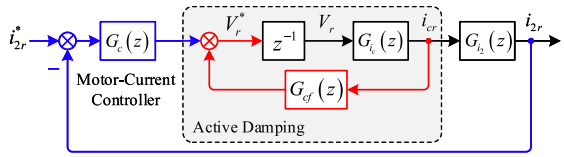

Fig. 15. Control diagram of the conventional capacitor-current-feedback AD methods [10], [21].

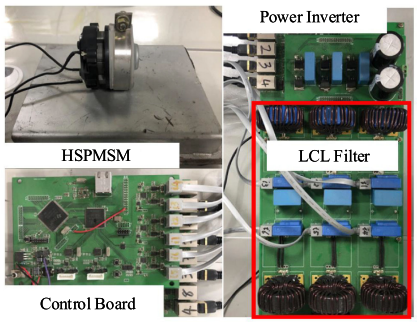

Fig. 16. Schematic diagram of the experimental setup.

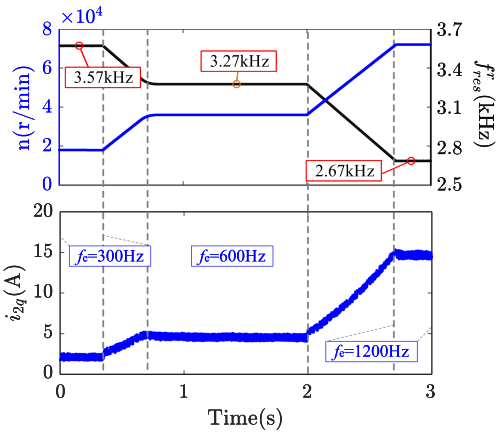

Fig. 17. Experimental results: AD performance with different speed. The synchronous resonance frequency f_{res}^r ranges from 3.57 to 2.67 kHz. $f_s/6 = 3.33$ kHz.

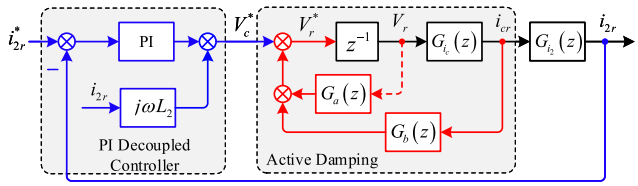

Fig. 18. Control structure of the conventional PI decoupled controller.

where f_{hp} is the cutoff frequency of the high-pass filter. Additionally, according to Parker *et al.* [10] and Wang *et al.* [21], the coefficients k_c and f_{hp} are selected as

$$k_c = 0.1, \quad f_{hp} = 5000. \tag{56}$$

Fig. 14(b) and (c) shows the AD performance with method in [10] and [21], respectively. In Fig. 14(b), as the speed up, the current control loop becomes unstable at $f_e = 867$ Hz. Besides, as shown in Fig. 14(b), the stability of the current control loop is only ensured within f_e=1133 Hz. Therefore, according to the aforementioned simulation results, the proposed AD method has a wider stable resonance region compared with the conventional methods, which is beneficial for the high-speed applications.

VI. Experimental Validations and Analysis

The experiment is designed to validate the effectiveness of the proposed method. The parameters of the experimental plant are shown in Table I. The parameters of the proposed method are shown in Table II. A fan is connected to the shaft of the tested motor as a load. The experimental setup is shown in Fig. 16. All the data of the experiments are sent to the host PC by the Ethernet module in the control board.

A. Synchronous AD Performance

Fig. 17 shows experimental results of the proposed capacitor-current-feedback AD performance with different speeds. With the speed controller, the motor speed ranges from 18 (300 Hz) to 36 kr/min (600 Hz), and then to 72 kr/min (1200 Hz). Correspondingly, the synchronous resonance frequency decreases from 3.57 to 3.27 kHz, and then to 2.67 kHz. Clearly, it moves across the critical synchronous resonance frequency

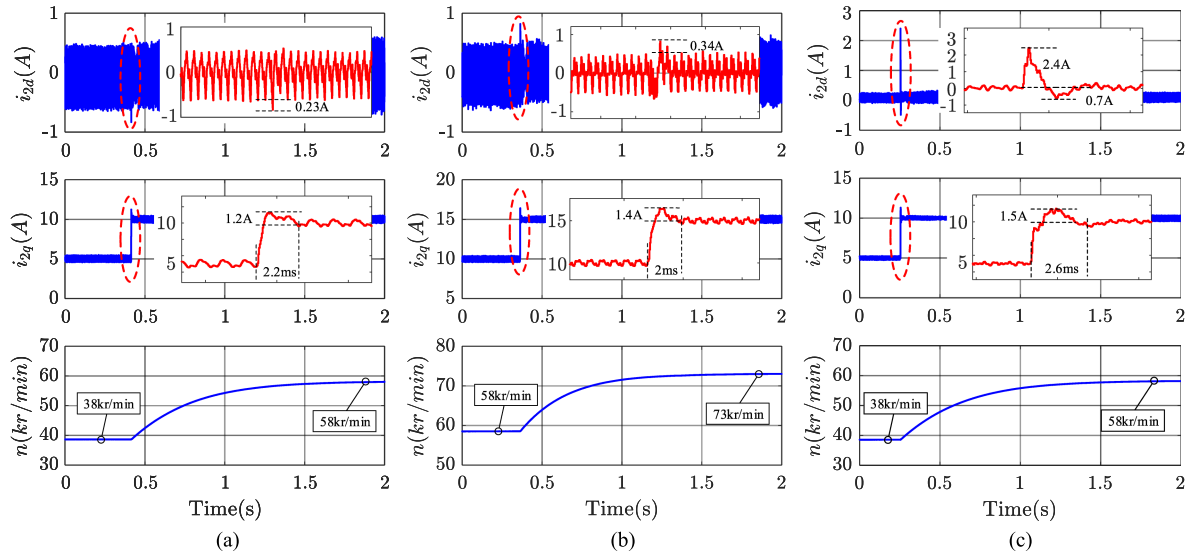

Fig. 19. Experimental results: the dynamic decoupling performance with the proposed method and conventional PI decoupled controller. From top to down: i_{2d}, i_{2q}, and speed (kr/min). (a) Proposed method: i_{2q} from 5 to 10 A. (b) Proposed method: i_{2q} from 10 to 15 A. (c) PI controller: i_{2q} from 5 to 10 A.

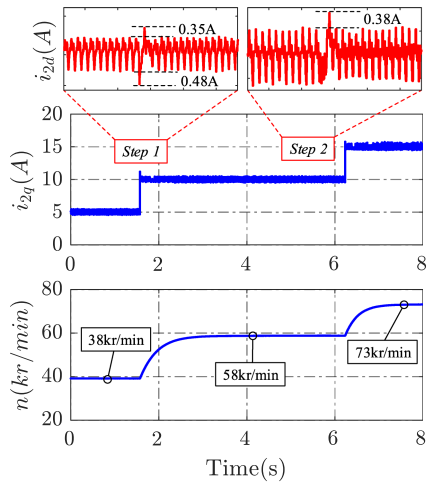

Fig. 20. Experimental results: the current control performance when the motor inductance adopted in the controller is 0.

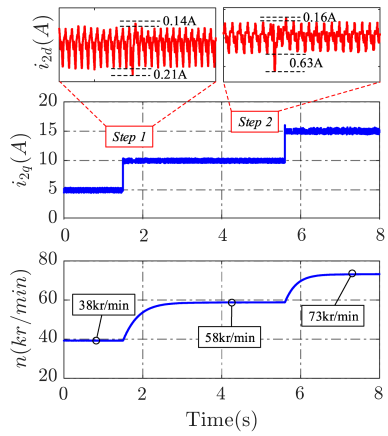

Fig. 21. Experimental results: the current control performance when the motor inductance adopted in the controller is $2L_s$.

[i.e., 3.062 kHz based on (19)]. It indicates that the proposed capacitor-current-feedback AD method is effective regardless of the resonance frequency.

B. Dynamic Decoupling Performance and Comparison

The current transient performances of the proposed current controller and the conventional PI controller (see Fig. 18) are compared. Fig. 19 shows the experimental results of the dynamic decoupling performance with the proposed method and conventional PI controller. $i_{2d}^* = 0$.

In Fig. 19(a), the current reference i_{2q}^* has a stepping increase from 5 to 10 A at $t = 0.43$ s and, thus, the speed of the tested motor varies from 38 (633.33 Hz) to 58 kr/min (967 Hz). It can be observed that the proposed method effectively tracks i_{2q}^* with a rise time of about 2.2 ms and a overshoot of about 1.2 A. With the stepping i_{2q}, the maximum deviation of i_{2d} is 0.23 A. In the high-speed region, as shown in Fig. 19(b), the current reference i_{2q}^* has a stepping change from 10 to 15 A at $t = 0.35$ s and, thus, the speed changes from 58 (967 Hz) to 73 kr/min (1217 Hz). The maximum deviation of i_{2d} is 0.34 A.

As a comparison, the current transient performance of the conventional PI controller is investigated, as shown in Fig. 19(c). The PI controller is designed with $k_p = 0.4$ and $k_i = 1000$. With the stepping i_{2q}^* from 5 to 10 A, the PI controller tracks i_{2q}^* with a rise time of about 2.6 ms and a overshoot of about 1.5 A. But the maximum deviation of i_{2d} is up to 2.4 A. When at a higher speed, the deviation of i_{2d} has to be increased inevitably.

Therefore, with the much reduced deviation of i_{2d}, the proposed current controller has a better dynamic-decoupled capability.

C. Robustness Validation

To validate the robustness of the proposed capacitor-current-feedback AD and the coefficient selection method against the

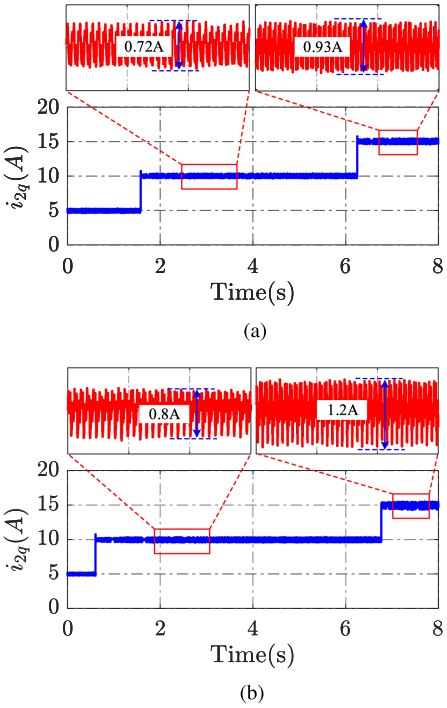

Fig. 22. Experimental results: current ripple of the proposed method with cases 1 and 2. (a) Case 1. (b) Case 2.

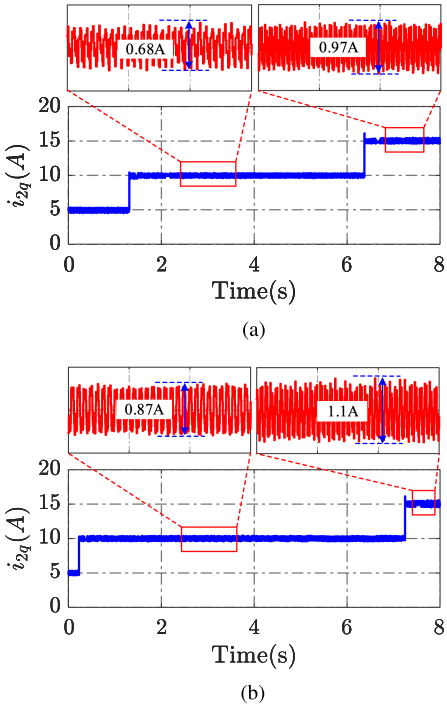

Fig. 23. Experimental results: current ripple of the proposed method with cases 3 and 4. (a) Case 3. (b) Case 4.

motor inductance variation, the motor inductance adopted in the controller is selected as 0 and $2L_s$, respectively.

Fig. 20 shows the experimental results of the current control performance of the proposed method when the motor inductance $L_s = 0$ is adopted in the controller. It can be observed that the closed-loop stability of the proposed method is still guaranteed when the motor is driven from 38 to 73 kr/min. At step 1 (5 to 10 A), the maximum deviation of i_{2d} is 0.48 A while 0.38 A at step 2 (10 to 15 A). In Fig. 21, the motor inductance $2L_s$ is adopted in the digital controller. At step 1 (5 to 10 A), the maximum deviation of i_{2d} is 0.21 A while 0.63 A at step 2 (10 to 15 A). According to the experimental results, the proposed current controller with the coefficient selection method works well, even when the motor inductance varies from 0% to 200% of the real inductance.

D. Different AD Coefficient Selections

The following cases are established to validate the analysis of the coefficient (i.e., $\overline{f}_{\text{res}}$, δ, and γ_2) selection in the proposed AD method.

1) Case 1: $\delta = 0.6$, $\overline{f}_{\text{res}} = 4800$ Hz, and $\gamma_2 = -0.3$.
2) Case 2: $\delta = 0.6$, $\overline{f}_{\text{res}} = 5500$ Hz, and $\gamma_2 = -0.3$.
3) Case 3: $\delta = 0.8$, $\overline{f}_{\text{res}} = 5500$ Hz, and $\gamma_2 = -0.1$.
4) Case 4: $\delta = 0.8$, $\overline{f}_{\text{res}} = 5500$ Hz, and $\gamma_2 = -0.5$.

As the analysis mentioned earlier, $\overline{f}_{\text{res}}$ and γ_2 should be selected appropriately based on (36) and (41) to enhance the suppression ability for the measurement noises. The current ripple of i_{2q} is evaluated.

Fig. 22 shows the current control performance with cases 1 and 2, where the desired resonance frequency $\overline{f}_{\text{res}}$ is different (4800 and 5500 Hz, respectively). At $i_{2q} = 10$ A, the absolute value of the current ripple is 0.72 A in case 1 while 0.8 A in case 2. At high speed ($i_{2q} = 15$ A), the current rippled increases to 0.93 A in case 1 while 1.2 A in case 2. It can be concluded that high $\overline{f}_{\text{res}}$ enlarges the current ripple, which is consistent with the theoretical analysis. Besides, δ is 0.6 in both cases 1 and 2, which indicates that the selection of δ is more flexible.

Fig. 23 shows the current control performance with cases 3 and 4, where different γ_2 is adopted (-0.1 and -0.5, respectively). At $i_{2q} = 10$ A, the absolute value of the current ripple is 0.68 A in case 3 while 0.87 A in case 4. At high speed ($i_{2q} = 15$ A), the current rippled increases to 0.97 A in case 3 while 1.1 A in case 4. Therefore, the large absolute value of γ_2 increases the current ripple, which is also consistent with the theoretical analysis.

VII. Conclusion

This article deals with the challenges of the synchronous current control for the *LCL*-equipped HSPMSM drive system: first, the synchronous resonance frequency varying in a wide range because of the synchronous transformation, and second, eliminating the coupling between the dq coordinate. Some improvements are achieved as follows.

1) Improved synchronous capacitor-current-feedback AD method based on the arbitrary pole assignment and, thus, the damping performance can be freely designed compared with the previous methods.
2) Effective for the *LCL* resonance within the Nyquist frequency ($f_s/2$).

3) Enhanced dynamic decoupling capability to improve the transient performance compared with the conventional PI decoupled method.
4) Benefiting from the discrete-time design, it works well in the high-speed region.

Finally, the effectiveness of the proposed method is verified by driving the tested motor to 72 kr/min.

APPENDIX

Based on (45), the following equation can be derived as

$$\sqrt{a^2+\left(\frac{a+b}{\omega T}\right)^2}\approx a,\ \omega>\omega_{cp} \tag{A.1}$$

$$a\tan\left(\frac{a+b}{\omega_{cg}Ta}\right)\approx 0 \tag{A.2}$$

where ω_{cg} is the frequency where the GM is measured, which is a -180° phase crossing frequency. Therefore, the magnitude and phase of the forward-path transfer function can be written as

$$\left|\frac{i_{2r}(z)}{i^e_{2r}(z)}\right|(z=e^{-j\omega T})\approx\frac{\eta}{\omega T}\frac{a}{\lambda_+(\omega,\omega_e)\lambda_-(\omega,\omega_e)}$$
$$\angle\frac{i_{2r}(z)}{i^e_{2r}(z)}(z=e^{-j\omega T})=-\frac{\pi}{2}-\frac{3}{2}\omega T-a\tan\left(\frac{a+b}{\omega Ta}\right). \tag{A.3}$$

To achieve PM$\geq\varphi$, it leads to

$$\left|\frac{i_{2r}(z)}{i^e_{2r}(z)}\right|(z=e^{-j\omega_{cp}T})=1 \tag{A.4}$$

$$\angle\frac{i_{2r}(z)}{i^e_{2r}(z)}(z=e^{-j\omega_{cp}T})+\pi=\varphi \tag{A.5}$$

where φ is the required PM. By appropriate math manipulations, it can be derived as

$$a=\frac{\lambda_+(\omega_{cp},\omega_e)\lambda_-(\omega_{cp},\omega_e)}{\eta}\omega_{cp}T$$
$$b=a\left(\omega_{cp}\tan\left(\frac{\pi}{2}-\frac{3\omega_{cp}T}{2}-\varphi\right)T-1\right). \tag{A.6}$$

For the GM, it needs

$$\angle\frac{i_{2r}(z)}{i^e_{2r}(z)}(z=e^{-j\omega_{cg}T})=\pi. \tag{A.7}$$

Considering (A.2), ω_{cg} can be calculated as

$$\omega_{cg}=\frac{\pi}{3T}. \tag{A.8}$$

At $\omega=\omega_{cg}$, the magnitude of the open-loop transfer function is required as

$$\left|\frac{i_{2r}(z)}{i^e_{2r}(z)}\right|(z=e^{-j\omega_{cg}T})<\frac{\sqrt{2}}{2}. \tag{A.9}$$

Therefore, the maximum a can be expressed as

$$a<\frac{\lambda_+(\frac{\pi}{3T},\omega_e)\lambda_-(\frac{\pi}{3T},\omega_e)}{\eta}\frac{\sqrt{2}\pi}{6T}. \tag{A.10}$$

Based on (A.6), ω_{cp} should meet as

$$\omega_{cp}<\frac{\sqrt{2}\pi}{6T}\frac{\lambda_+(\frac{\pi}{3T},\omega_e)\lambda_-(\frac{\pi}{3T},\omega_e)}{\lambda_+(\omega_{cp},\omega_e)\lambda_-(\omega_{cp},\omega_e)}. \tag{A.11}$$

It should be noted that $\omega_{cp}T$ is much less than ρ and, thus, it results in

$$\omega_{cp}<\frac{\sqrt{2}\pi}{6T}\frac{\lambda_+(\frac{\pi}{3T},\omega_e)\lambda_-(\frac{\pi}{3T},\omega_e)}{\lambda_+(0,\omega_e)\lambda_-(0,\omega_e)}. \tag{A.12}$$

It can be checked that the minimum value of the aforementioned equation can be obtained when the maximum ω_e is adopted and, thus, it leads to

$$\omega_{cp}<\frac{\sqrt{2}\pi}{6T}\frac{\lambda_+(\frac{\pi}{3T},\omega^m_e)\lambda_-(\frac{\pi}{3T},\omega^m_e)}{\lambda_+(0,\omega^m_e)\lambda_-(0,\omega^m_e)} \tag{A.13}$$

where ω^m_e is the maximum fundamental angular frequency of the machine.

REFERENCES

[1] D. Gerada, A. Mebarki, N. L. Brown, C. Gerada, A. Cavagnino, and A. Boglietti, "High-speed electrical machines: Technologies, trends, and developments," *IEEE Trans. Ind. Electron.*, vol. 61, no. 6, pp. 2946–2959, Jun. 2014.

[2] J. Wang, J. D. Yan, L. Jiang, and J. Zou, "Delay-dependent stability of single-loop controlled grid-connected inverters with LCL filters," *IEEE Trans. Power Electron.*, vol. 31, no. 1, pp. 743–757, Jan. 2016.

[3] C. Zou, B. Liu, S. Duan, and R. Li, "Influence of delay on system stability and delay optimization of grid-connected inverters with LCL filter," *IEEE Trans. Ind. Informat.*, vol. 10, no. 3, pp. 1775–1784, Aug. 2014.

[4] J. Yin, S. Duan, and B. Liu, "Stability analysis of grid-connected inverter with LCL filter adopting a digital single-loop controller with inherent damping characteristic," *IEEE Trans. Ind. Informat.*, vol. 9, no. 2, pp. 1104–1112, May 2013.

[5] Y. Tang, P. C. Loh, P. Wang, F. H. Choo, and F. Gao, "Exploring inherent damping characteristic of LCL-filters for three-phase grid-connected voltage source inverters," *IEEE Trans. Power Electron.*, vol. 27, no. 3, pp. 1433–1443, Mar. 2012.

[6] J. Dannehl, M. Liserre, and F. W. Fuchs, "Filter-based active damping of voltage source converters with LCL filter," *IEEE Trans. Ind. Electron.*, vol. 58, no. 8, pp. 3623–3633, Aug. 2011.

[7] W. Yao, Y. Yang, X. Zhang, F. Blaabjerg, and P. C. Loh, "Design and analysis of robust active damping for LCL filters using digital notch filters," *IEEE Trans. Power Electron.*, vol. 32, no. 3, pp. 2360–2375, Mar. 2017.

[8] R. A. Fantino, C. A. Busada, and J. A. Solsona, "Optimum PR control applied to LCL filters with low resonance frequency," *IEEE Trans. Power Electron.*, vol. 33, no. 1, pp. 793–801, Jan. 2018.

[9] E. Rodriguez-Diaz, F. D. Freijedo, J. C. Vasquez, and J. M. Guerrero, "Analysis and comparison of notch filter and capacitor voltage feedforward active damping techniques for LCL grid-connected converters," *IEEE Trans. Power Electron.*, vol. 34, no. 4, pp. 3958–3972, Apr. 2019.

[10] S. G. Parker, B. P. McGrath, and D. G. Holmes, "Regions of active damping control for LCL filters," *IEEE Trans. Ind. Appl.*, vol. 50, no. 1, pp. 424–432, Jan./Feb. 2014.

[11] M. B. Saïd-Romdhane, M. W. Naouar, I. Slama-Belkhodja, and E. Monmasson, "Robust active damping methods for LCL filter-based grid-connected converters," *IEEE Trans. Power Electron.*, vol. 32, no. 9, pp. 6739–6750, Sep. 2017.

[12] X. Wang, C. Bao, X. Ruan, W. Li, and D. Pan, "Design considerations of digitally controlled LCL-filtered inverter with capacitor- current-feedback active damping," *IEEE J. Emerg. Sel. Topics Power Electron.*, vol. 2, no. 4, pp. 972–984, Dec. 2014.

[13] J. Kukkola, M. Hinkkanen, and K. Zenger, "Observer-based state-space current controller for a grid converter equipped with an LCL filter: Analytical method for direct discrete-time design," *IEEE Trans. Ind. Appl.*, vol. 51, no. 5, pp. 4079–4090, Sep./Oct. 2015.

[14] E. Wu and P. W. Lehn, "Digital current control of a voltage source converter with active damping of LCL resonance," *IEEE Trans. Power Electron.*, vol. 21, no. 5, pp. 1364–1373, Sep. 2006.

[15] C. A. Busada, S. G. Jorge, and J. A. Solsona, "Full-state feedback equivalent controller for active damping in LCL-filtered grid-connected inverters using a reduced number of sensors," *IEEE Trans. Ind. Electron.*, vol. 62, no. 10, pp. 5993–6002, Oct. 2015.
[16] J. Dannehl, F. W. Fuchs, and P. B. Thøgersen, "PI state space current control of grid-connected PWM converters with LCL filters," *IEEE Trans. Power Electron.*, vol. 25, no. 9, pp. 2320–2330, Sep. 2010.
[17] R. Guzman, L. G. de Vicuña, J. Morales, M. Castilla, and J. Miret, "Model-based active damping control for three-phase voltage source inverters with LCL filter," *IEEE Trans. Power Electron.*, vol. 32, no. 7, pp. 5637–5650, Jul. 2017.
[18] G. G. Koch, L. A. Maccari, R. C. L. F. Oliveira, and V. F. Montagner, "Robust $\mathcal{H}_\infty$ state feedback controllers based on linear matrix inequalities applied to grid-connected converters," *IEEE Trans. Ind. Electron.*, vol. 66, no. 8, pp. 6021–6031, Aug. 2019.
[19] W. Wu, Y. Liu, Y. He, H. S. H. Chung, M. Liserre, and F. Blaabjerg, "Damping methods for resonances caused by LCL-filter-based current-controlled grid-tied power inverters: An overview," *IEEE Trans. Ind. Electron.*, vol. 64, no. 9, pp. 7402–7413, Sep. 2017.
[20] D. Pan, X. Ruan, C. Bao, W. Li, and X. Wang, "Capacitor-current-feedback active damping with reduced computation delay for improving robustness of LCL-type grid-connected inverter," *IEEE Trans. Power Electron.*, vol. 29, no. 7, pp. 3414–3427, Jul. 2014.
[21] X. Wang, F. Blaabjerg, and P. C. Loh, "Virtual RC damping of LCL-filtered voltage source converters with extended selective harmonic compensation," *IEEE Trans. Power Electron.*, vol. 30, no. 9, pp. 4726–4737, Sep. 2015.
[22] X. Li, X. Wu, Y. Geng, X. Yuan, C. Xia, and X. Zhang, "Wide damping region for LCL-type grid-connected inverter with an improved capacitor-current-feedback method," *IEEE Trans. Power Electron.*, vol. 30, no. 9, pp. 5247–5259, Sep. 2015.
[23] D. Pan, X. Ruan, C. Bao, W. Li, and X. Wang, "Optimized controller design for LCL-type grid-connected inverter to achieve high robustness against grid-impedance variation," *IEEE Trans. Ind. Electron.*, vol. 62, no. 3, pp. 1537–1547, Mar. 2015.
[24] Y. He, X. Wang, X. Ruan, D. Pan, X. Xu, and F. Liu, "Capacitor-current proportional-integral positive feedback active damping for LCL-type grid-connected inverter to achieve high robustness against grid impedance variation," *IEEE Trans. Power Electron.*, vol. 34, no. 12, pp. 12 423–12436, Dec. 2019.
[25] H. Kim, M. W. Degner, J. M. Guerrero, F. Briz, and R. D. Lorenz, "Discrete-time current regulator design for AC machine drives," *IEEE Trans. Ind. Appl.*, vol. 46, no. 4, pp. 1425–1435, Jul./Aug. 2010.

Yu Yao (Student Member, IEEE) received the B.S. degree in electrical engineering in 2016 from Southeast University, Nanjing, China, where he is currently working toward the Dr. Eng. degree in electric machines and control with the School of Electrical Engineering.

His main research interests include the design of the power inverter, current regulator design, position sensorless drive for the high-speed PSMSM, and active damping methods for the high-speed drive system with *LCL* output filter.

Yunkai Huang received the M.Sc. and Ph.D. degrees in electrical engineering from Southeast University, Nanjing, China, in 2001 and 2007, respectively.

He is currently a Professor with the School of Electrical Engineering, Southeast University. His research interests include design and control of PM machine and high-speed machine, applications in domestic appliances, electric vehicles, railway traction, all-electric ships, more-electric aircraft, and wind power generation systems.

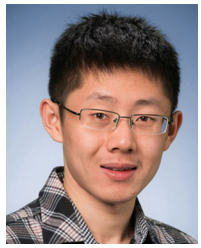

Fei Peng (Member, IEEE) received the B.S. and M.S. degrees in electrical engineering from Southeast University, Nanjing, China, in 2010 and 2012, respectively, and the Ph.D. degree in electrical and computer engineering from McMaster University, Hamilton, ON, Canada, in 2016.

He was a Postdoctoral Fellow with the McMaster Institute for Automotive Research and Technology, McMaster University. In December 2016, he joined the School of Electrical Engineering, Southeast University, as an Assistant Professor. His research interests include optimal design and control of power converters, and modeling and digital control of motor drives.

Jianning Dong (Member, IEEE) received the B.S. and Ph.D. degrees in electrical engineering from Southeast University, Nanjing, China, in 2010 and 2015, respectively.

Since 2016, he has been an Assistant Professor with the Delft University of Technology, Delft, The Netherlands. Before joining TU Delft, he was a Postdoctoral Researcher with McMaster Automotive Resource Centre, McMaster University, Hamilton, ON, Canada. His main research interests include design, modeling, and control of electromechanical systems.

Zichong Zhu (Student Member, IEEE) received the B.S. degree in thermal energy and power engineering from the Nanjing Institute of Technology, Nanjing, China, in 2014, and the Ph.D. degree in electrical engineering from Southeast University, Nanjing, China, in 2021.

He joined Nanjing Tech University, Nanjing, China, as a Lecturer in 2021. His research interests include electromagnetic analysis, thermal management and structural design of the permanent magnet synchronous machines for the wheel-hub driving, and turbo and servo applications.